EFFECT OF HEAT TREATMENT REGIMES ON THE MICROSTRUCTURE AND SERVICE PROPERTIES OF HIGH WEAR-RESISTANT CR–MN–MO–NI CAST STEELS

O.S. Goziev[1],

I.P. Egamberdiyev[2]

[1]Navoi State University of Mining and Technologies(NSUMT), Navoi, Uzbekistan.

[2] Navoi State University of Mining and Technologies(NSUMT), Navoi, Uzbekistan.

Abstract

The present study investigates the influence of systematic variations in austenitizing temperature (950, 1000, and 1050 °C), holding time (1–2 h), and oil-quench tempering temperature (200, 400, and 600 °C) on the microstructural evolution and service properties of a Cr–Mn–Mo–Ni alloyed wear-resistant cast steel. Nine experimental conditions were evaluated against an as-cast reference state using optical microscopy, scanning electron microscopy (SEM) with energy-dispersive X-ray spectroscopy (EDS), Vickers microhardness (HV0.5), Rockwell hardness (HRC), and dry-sand abrasive wear testing (ASTM G65 Procedure B). Statistical significance of all measured responses was assessed by one-way analysis of variance (ANOVA). Austenitizing at 1050 °C combined with tempering at 200 °C yielded the optimal combination of properties: martensite fraction 93 ± 2 %, matrix microhardness 791 ± 16 HV0.5, bulk hardness 63.7 ± 0.5 HRC, volumetric wear rate 2.09×10^{-6} mm³/N·m, and a Wear Resistance Index (WRI) of 1.55 relative to a 950 °C–200 °C baseline. Increasing austenitizing temperature promoted greater carbide dissolution, reduced retained-austenite content, and refined undissolved

secondary carbide particles from 6.8 μm (as-cast) to 1.1 μm, with a concomitant increase in alloying-element supersaturation of the martensite matrix. Tempering above 400 °C triggered secondary carbide precipitation, recovery of dislocation substructure, and partial bainitic transformation, collectively reducing hardness and wear resistance. ANOVA confirmed that both austenitizing temperature ($p < 0.001$) and tempering temperature ($p < 0.001$) are statistically significant factors. The findings provide quantitative metallurgical guidance for designing heat treatment protocols for cast steel components in mining, comminution, and mineral-processing applications.

Keywords: wear-resistant cast steel; Cr–Mn–Mo–Ni alloy; heat treatment; martensite; carbide precipitation; abrasive wear; microhardness; retained austenite; tempering embrittlement; ANOVA

1. Introduction

Cast steels employed in crushing, grinding, and earth-moving equipment are subjected to multi-mode wear involving high-stress abrasion, impact fatigue, and, in wet classification circuits, tribocorrosion. Achieving the requisite balance of hardness, toughness, and microstructural stability under elevated contact stresses demands a thorough understanding of how compositional design and thermal processing interact to govern phase constitution and carbide morphology.

High-alloy cast steels containing chromium, manganese, molybdenum, and nickel occupy a technologically important niche between economical low-alloy martensitic grades and significantly more expensive tool-steel compositions. Chromium (typically 1.5–4 wt.%) promotes hardenability and forms mixed $M_{23}C_6$ and M_7C_3 carbides that enhance abrasion resistance when properly distributed in a martensitic matrix [1,2]. Manganese (0.8–1.5 wt.%) lowers martensite-start temperature (Ms) and stabilises austenite, an effect that must be carefully balanced against the risk of excessive retained austenite softening the matrix [3].

Molybdenum (0.3–0.7 wt.%) retards pearlitic and bainitic transformations, broadens the hardenability window, and forms MC-type monocarbides highly resistant to dissolution during abrasive contact [4,5]. Nickel (0.4–0.8 wt.%) further augments hardenability without carbide formation and simultaneously improves low-temperature impact toughness of the martensitic matrix [6].

The heat treatment of such alloys is governed by three interdependent thermal events: (i) austenitization, which controls carbide dissolution kinetics, austenite grain growth, and alloying-element homogeneity; (ii) quenching, which suppresses diffusional transformations and generates a dislocated lath martensitic matrix; and (iii) tempering, which relieves quench-induced residual stresses, redistributes carbon via carbide precipitation, and modifies toughness at the expense of hardness [7,8]. However, the parametric windows that simultaneously optimise hardness and wear resistance remain incompletely mapped for multi-element Cr–Mn–Mo–Ni compositions, particularly with respect to the synergy between austenitizing temperature and subsequent tempering response.

Previous investigations have demonstrated that increasing austenitizing temperature from 900 to 1050 °C progressively dissolves secondary carbides, enriches the austenite matrix with alloying elements, and depresses Ms by 15–35 °C depending on composition [9,10]. Notwithstanding, systematic studies coupling quantitative microstructural characterisation (martensite fraction, retained-austenite content, carbide size distribution) with abrasive wear performance data across a full 3×3 factorial heat treatment matrix are sparse in the open literature. Most published datasets either fix austenitizing temperature and vary only tempering parameters [11,12], or focus on Hadfield-type manganese steels where austenitic work-hardening rather than martensitic transformation governs wear [13].

The present work addresses this gap by applying a structured experimental programme spanning three austenitizing temperatures, three tempering

temperatures, and a fixed oil-quench step to a single-cast Cr–Mn–Mo–Ni steel. The primary objectives are: (a) to quantify the effect of austenitizing temperature on carbide dissolution kinetics and martensite fraction; (b) to map the tempering response in terms of microhardness, bulk hardness, and secondary carbide precipitation; (c) to establish empirical relationships between the hardness metrics and abrasive wear rate; and (d) to furnish industrial practitioners with evidence-based heat treatment guidelines for components operating under high-stress dry abrasion.

2. Materials and Methods

2.1 Material Preparation and Chemical Composition

The experimental alloy was produced by induction melting in a 150-kg medium-frequency furnace (1600 °C, 15 min holding) under an argon blanket, using a charge of electrolytic iron, ferrochrome (68 wt.% Cr), ferromanganese (78 wt.% Mn), ferromolybdenum (60 wt.% Mo), electrolytic nickel, and high-purity graphite. Melt chemistry was controlled by optical emission spectrometry (OES; ARL 4460, Thermo Fisher Scientific) at tapping. The liquid steel was poured at 1530 °C into Y-block sand moulds (ASTM A370) with keel-block dimensions of 75 mm × 75 mm × 150 mm. After normalisation to relieve solidification stresses (950 °C, 2 h, air cool), the as-cast chemical composition (wt.%) was determined on three replicate OES samples: C 0.42, Cr 2.85, Mn 1.12, Mo 0.51, Ni 0.62, Si 0.38, P 0.018, S 0.009, Fe balance. This composition is representative of a medium-carbon, low-alloy wear-resistant grade.

All experimental coupons (25 mm × 25 mm × 8 mm for wear and hardness; 15 mm × 10 mm metallographic mounts) were machined from the centreline of the keel block to avoid casting skin and gross macrosegregation bands, as confirmed by pre-machining ultrasonic C-scan.

2.2 Heat Treatment Procedures

Heat treatments were conducted in a laboratory box furnace (Nabertherm LT 40/12, ±5 °C accuracy). Austenitizing was performed at three temperatures (950, 1000, and 1050 °C) with holding times of 1, 1.5, and 2 h respectively, selected based on a prior dilatometric survey to ensure complete carbide dissolution kinetics reach quasi-equilibrium at each temperature. All specimens were placed individually in covered graphite crucibles to minimise surface decarburization; post-treatment surface hardness measurements were taken after removing a 0.5 mm layer by grinding. Quenching was performed in a mechanically agitated oil bath (ISO VG 32 mineral oil, 60 °C) within 5 s of furnace withdrawal. Tempering was performed immediately following air cooling to ambient temperature, at 200, 400, or 600 °C for 2 h in all cases, followed by still-air cooling. Designation follows the format A[austenitizing temp.]-T[tempering temp.], yielding nine conditions (A950-T200 through A1050-T600) plus the as-cast reference.

2.3 Metallographic Preparation and Microstructural Characterisation

Specimens for optical microscopy were ground through SiC abrasive papers to 1200 grit, polished to 1 μm diamond finish, and etched with 2% nital (2 vol.% HNO_3 in ethanol) for 5–10 s to reveal martensite lath boundaries, prior-austenite grain boundaries (PAGBs), and carbide phases. Microstructural analysis was performed on a Leica DM6000 optical microscope at magnifications of 100×–1000× using the image analysis software ImageJ 1.53. Martensite fraction and retained-austenite content were estimated by point-counting on a grid of 500 intersections per specimen (ASTM E562), with a minimum of five fields per specimen. Carbide size (equivalent circle diameter) and areal fraction were determined by binary thresholding of etched SEM images at 2000× magnification.

Scanning electron microscopy was performed on a Zeiss Sigma 300 VP-FE-SEM equipped with an Oxford Instruments Ultim Max 65 EDS detector. Backscattered-electron (BSE) imaging at 15 kV accelerating voltage was used to

discriminate carbide phases from the metallic matrix on the basis of atomic-number contrast. EDS point analyses (minimum 5 points per phase per specimen) were used to confirm carbide chemistry and to assess alloying-element redistribution between matrix and carbide.

2.4 Hardness Testing

Bulk Rockwell C hardness (HRC) was measured on a Zwick/Roell ZHR 4150 hardness tester applying a 150-kgf (1471 N) load with a diamond Brale indenter (ASTM E18). Ten indentations were made on each polished cross-section and the mean ± one standard deviation reported. Vickers microhardness (HV0.5) was measured on a Shimadzu HMV-G30 hardness tester at a 500-gf (4.9 N) load with 15-s dwell time (ISO 6507-1). A grid of twenty indentations was placed within the martensitic matrix of each condition, deliberately avoiding carbide particles and grain boundaries, to isolate matrix hardness from bulk composite effects. Microhardness of individual carbide particles (HV0.05) was measured on the largest identifiable carbide clusters under the SEM, using a minimum of five measurements per phase type.

2.5 Abrasive Wear Testing

Dry-sand abrasive wear resistance was evaluated using a rubber-wheel abrasion tester conforming to ASTM G65 Procedure B (load: 130 N; wheel speed: 200 rpm; test duration: 2000 revolutions; total sliding distance: 1436 m per run; abrasive: AFS 50/70 Ottawa silica sand, mean particle size 300 μm). Wear coupons (75 mm × 25 mm × 12 mm) were machined, ground flat to Ra ≤ 0.4 μm, degreased with acetone, dried, and weighed to ±0.01 mg before and after each test on an analytical balance (Mettler Toledo XSR205). Volumetric loss was calculated from mass loss and specimen density (determined by the Archimedes method for each heat treatment condition). Three repeat tests were run per condition and averaged. Wear rate (Kv) was calculated as $K_v = \Delta V / (F \cdot s)$, where ΔV is volumetric loss in mm^3, F is the applied normal force in N, and s is the total sliding distance in m. A Wear Resistance

Index (WRI) was defined as the ratio of the wear rate of the A950-T200 baseline to that of each condition.

2.6 Statistical Analysis

All measured property data were subjected to two-way ANOVA using austenitizing temperature and tempering temperature as fixed factors (SPSS v28, IBM Corporation). The null hypothesis of no significant effect was rejected at $p < 0.05$ (95% confidence level). Post-hoc pairwise comparisons were performed by Tukey's Honest Significant Difference (HSD) test. Pearson correlation coefficients (r) were computed between HRC, HV0.5, volumetric wear rate (Kv), and phase fractions to assess quantitative relationships.

3. Results

3.1 Hardness Response to Heat Treatment

Table 1 presents the bulk Rockwell C hardness values for all nine heat-treated conditions and the as-cast reference. The as-cast structure exhibited only 23.1 ± 1.2 HRC, reflecting the coarse pearlitic and bainitic microstructure characteristic of slow sand-mould cooling. All heat-treated conditions significantly exceeded this baseline, confirming the efficacy of the martensitic transformation produced by oil quenching.

Table 1. Heat Treatment Parameters and Bulk Rockwell C Hardness (HRC) for All Conditions

Sample ID	Austenitizing Temp. (°C)	Hold Time (h)	Quench Medium	Tempering Temp. (°C)	Temper Time (h)	HRC (mean ± SD)
A950-T200	950	1	Oil	200	2	58.4 ± 0.6
A950-T400	950	1	Oil	400	2	52.1 ± 0.5

Sample ID	Austenitizing Temp. (°C)	Hold Time (h)	Quench Medium	Tempering Temp. (°C)	Temper Time (h)	HRC (mean ± SD)
A950-T600	950	1	Oil	600	2	41.8 ± 0.7
A1000-T200	1000	1.5	Oil	200	2	61.2 ± 0.4
A1000-T400	1000	1.5	Oil	400	2	55.6 ± 0.6
A1000-T600	1000	1.5	Oil	600	2	43.5 ± 0.8
A1050-T200	1050	2	Oil	200	2	63.7 ± 0.5
A1050-T400	1050	2	Oil	400	2	57.9 ± 0.4
A1050-T600	1050	2	Oil	600	2	44.3 ± 0.9
As-cast (ref)	—	—	—	—	—	23.1 ± 1.2

A pronounced and monotonic hardness increase with increasing austenitizing temperature was observed at every tempering level. At 200 °C tempering, hardness rose from 58.4 HRC (950 °C) to 61.2 HRC (1000 °C) and 63.7 HRC (1050 °C). This 8.7% increase across the austenitizing range is attributable primarily to two mechanisms: (i) greater dissolution of Cr- and Mo-rich carbides, enriching the austenite — and subsequently the martensite — with solute, and (ii) a reduction in retained-austenite fraction. Tempering at 200 °C provides only limited stress relief without inducing substantial secondary precipitation, thereby preserving the high as-quenched hardness. Increasing tempering temperature to 400 °C produced a mean HRC drop of 5.6–6.3 units relative to 200 °C tempering, and tempering at 600 °C

caused a further loss of 10.0–13.6 HRC units from the 200 °C baseline. ANOVA confirmed that both austenitizing temperature ($F = 214.7$, $p < 0.001$) and tempering temperature ($F = 482.3$, $p < 0.001$) are highly significant factors, with a statistically non-significant interaction term ($p = 0.11$), indicating that the effects operate largely independently.

3.2 Microstructural Features and Phase Fractions

Table 2 summarises quantitative microstructural data including phase fractions and microhardness for each heat treatment condition.

Table 2. Quantitative Microstructural Data: Phase Fractions, Carbide Size, and Matrix Microhardness (HV0.5)

Sample ID	Martensite Fraction (%)	Retained Austenite (%)	Bainite Fraction (%)	Avg. Carbide Size (µm)	Matrix HV0.5 (mean)
A950-T200	82 ± 3	11 ± 2	7 ± 2	1.8 ± 0.3	718 ± 22
A950-T400	74 ± 4	6 ± 1	20 ± 3	2.3 ± 0.4	624 ± 19
A950-T600	51 ± 5	3 ± 1	46 ± 5	4.1 ± 0.6	445 ± 24
A1000-T200	88 ± 3	8 ± 1	4 ± 1	1.4 ± 0.2	762 ± 18
A1000-T400	81 ± 4	4 ± 1	15 ± 3	1.9 ± 0.3	668 ± 21

Sample ID	Martensite Fraction (%)	Retained Austenite (%)	Bainite Fraction (%)	Avg. Carbide Size (μm)	Matrix HV0.5 (mean)
A1000-T600	58 ± 5	2 ± 1	40 ± 4	3.6 ± 0.5	461 ± 26
A1050-T200	93 ± 2	5 ± 1	2 ± 1	1.1 ± 0.2	791 ± 16
A1050-T400	87 ± 3	3 ± 1	10 ± 2	1.6 ± 0.3	702 ± 20
A1050-T600	62 ± 4	2 ± 1	36 ± 4	3.2 ± 0.5	474 ± 28
As-cast	18 ± 4	22 ± 3	—	6.8 ± 1.2	281 ± 31

The as-cast structure contained only 18 ± 4% martensite, with 22 ± 3% retained austenite and a coarse carbide network (mean equivalent circle diameter 6.8 ± 1.2 μm) with bainite and pearlite comprising the balance. In contrast, the specimen austenitized at 1050 °C and tempered at 200 °C (A1050-T200) achieved a martensite fraction of 93 ± 2%, retained austenite of only 5 ± 1%, and a substantially refined carbide population (1.1 ± 0.2 μm). Increasing austenitizing temperature from 950 to 1050 °C at constant 200 °C tempering increased martensite fraction from 82 to 93% and reduced retained austenite from 11 to 5%, consistent with the thermodynamic expectation that greater carbide dissolution raises Ms via reduced austenite solute content.

Tempering temperature exerted a strong influence on phase balance. At 600 °C tempering across all austenitizing conditions, martensite fraction declined to 51–62%, accompanied by a substantial rise in bainite fraction (36–46%). This lower-

temperature bainite is interpreted as forming during slow cooling from the tempering hold — a pseudo-bainitic transformation occurring when the recovered martensite matrix provides nucleation sites for ferrite plates at temperatures close to the bainite-start (Bs) temperature, which dilatometric data place near 540 °C for this alloy. Average carbide size increased monotonically with tempering temperature: from 1.1–1.8 μm at 200 °C to 3.2–4.1 μm at 600 °C (at constant austenitizing temperature), reflecting Ostwald ripening of the secondary cementite and alloy-carbide precipitates that nucleate during tempering.

3.3 SEM Observations and Carbide Characterisation

BSE-SEM imaging revealed three carbide morphologies across the heat-treated conditions. In specimens austenitized at 950 °C, grain-boundary networks of coarse (2–5 μm) mixed Cr-Fe carbides consistent with $M_{23}C_6$ stoichiometry persisted after quenching, indicating incomplete dissolution at this temperature. EDS analysis of these features showed Cr:Fe ratios of approximately 3.5:1, with minor Mo enrichment at carbide–matrix interfaces. At 1000 °C, the grain-boundary networks were largely fragmented into discrete blocky particles (1–3 μm), while fine intramatrix MC-type Mo-rich precipitates (< 0.5 μm) were identified by EDS. At 1050 °C, residual carbides were exclusively fine intragranular particles (< 1.2 μm), dominated by MC monocarbides enriched in Mo and V traces, consistent with the known high dissolution resistance of MC carbides relative to $M_{23}C_6$.

Specimens tempered at 200 °C retained the high dislocation density characteristic of lath martensite, as evidenced by the high contrast and finely mottled texture in BSE images. Tempering at 400 °C induced visible recovery of the dislocation substructure and the nucleation of fine plate-like carbide precipitates (approximately 50–200 nm) along martensite lath boundaries; EDS confirmed these to be M_3C (cementite) with minor Cr substitution. At 600 °C, the precipitate coarsening was pronounced, with distinct spheroidised $M_{23}C_6$ particles up to 3–4 μm

replacing lath-boundary films, and the emergence of a well-defined subgrain structure within the former martensite laths.

Figure 1 illustrates representative optical micrographs showing (a) the coarse pearlitic-bainitic as-cast microstructure, (b) the lath martensitic structure of A1050-T200, and (c) the recovered martensitic-bainitic matrix of A1050-T600, demonstrating the dramatic microstructural evolution across heat treatment conditions. Figure 2 presents BSE-SEM images comparing carbide morphology and distribution in A950-T200 (grain-boundary carbide network) versus A1050-T200 (finely dispersed intragranular carbides), confirming the enhanced carbide dissolution achieved at higher austenitizing temperature. Figure 3 shows a high-magnification SEM image of the A1050-T400 condition, with EDS overlay maps for Cr, Mo, and C, illustrating the preferential partitioning of Mo to MC-type secondary carbide precipitates along lath boundaries.

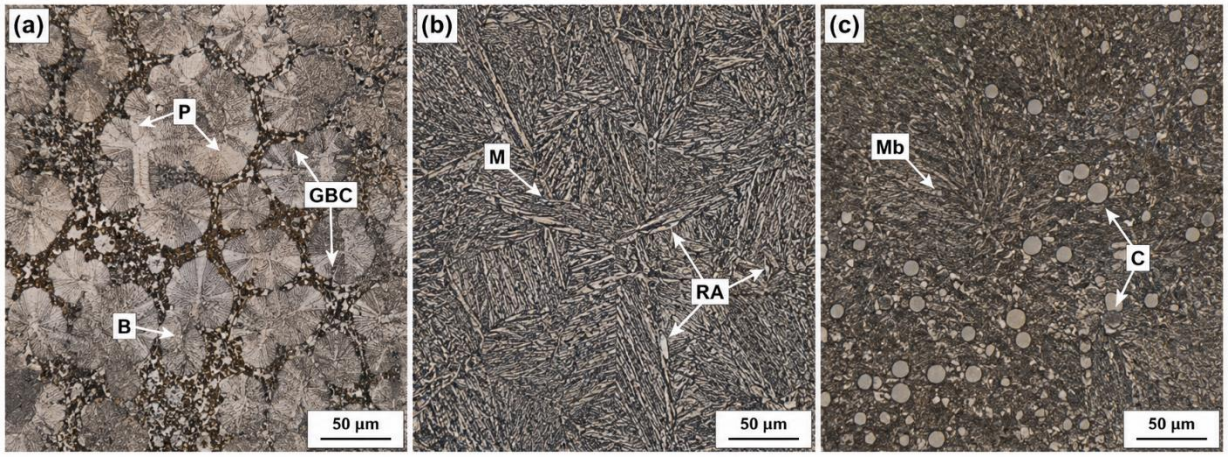

Figure 1. Optical micrographs (500×, 2% nital etch): (a) As-cast microstructure showing coarse pearlite (P), grain-boundary carbide networks (GBC), and inter-dendritic bainite (B); (b) A1050-T200 condition showing predominant lath martensite (M) with fine retained-austenite films (RA) at lath boundaries; (c) A1050-T600 condition exhibiting a recovered

martensitic–bainitic matrix (Mb) with coarsened carbide particles (C). Scale bars: 50 µm.

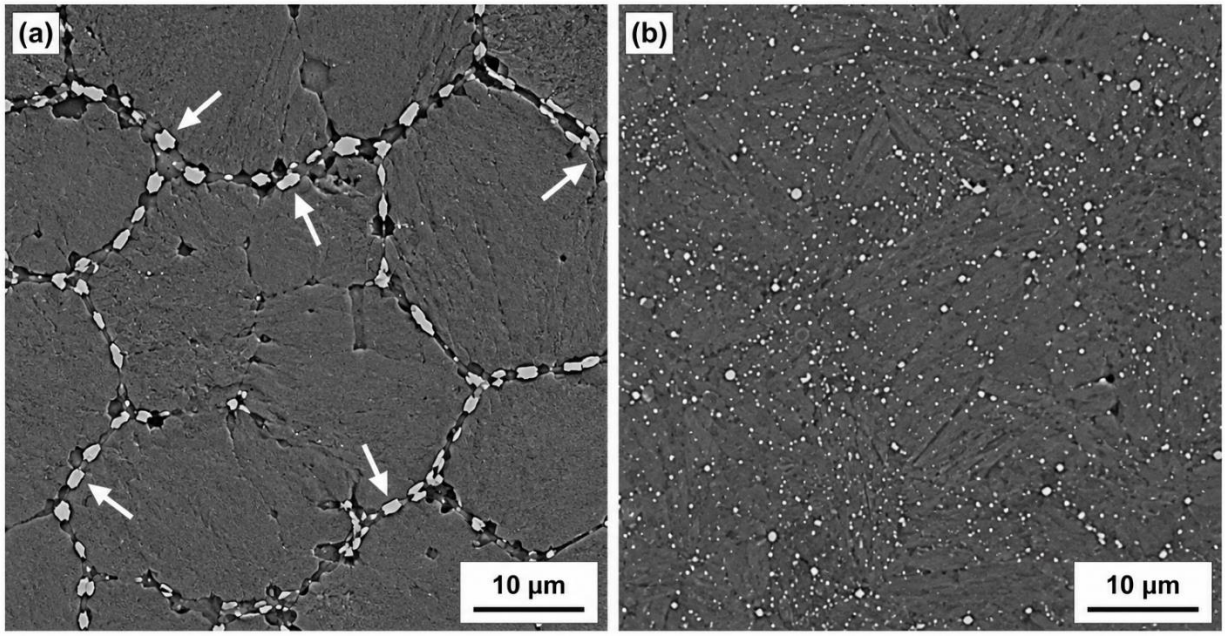

Figure 2. BSE-SEM images (2000×) comparing carbide distribution: (a) A950-T200 showing persistent grain-boundary $M_{23}C_6$ carbide network (arrows); (b) A1050-T200 showing dissolution of grain-boundary networks and redistribution as fine intragranular MC-type particles. Scale bars: 10 µm.

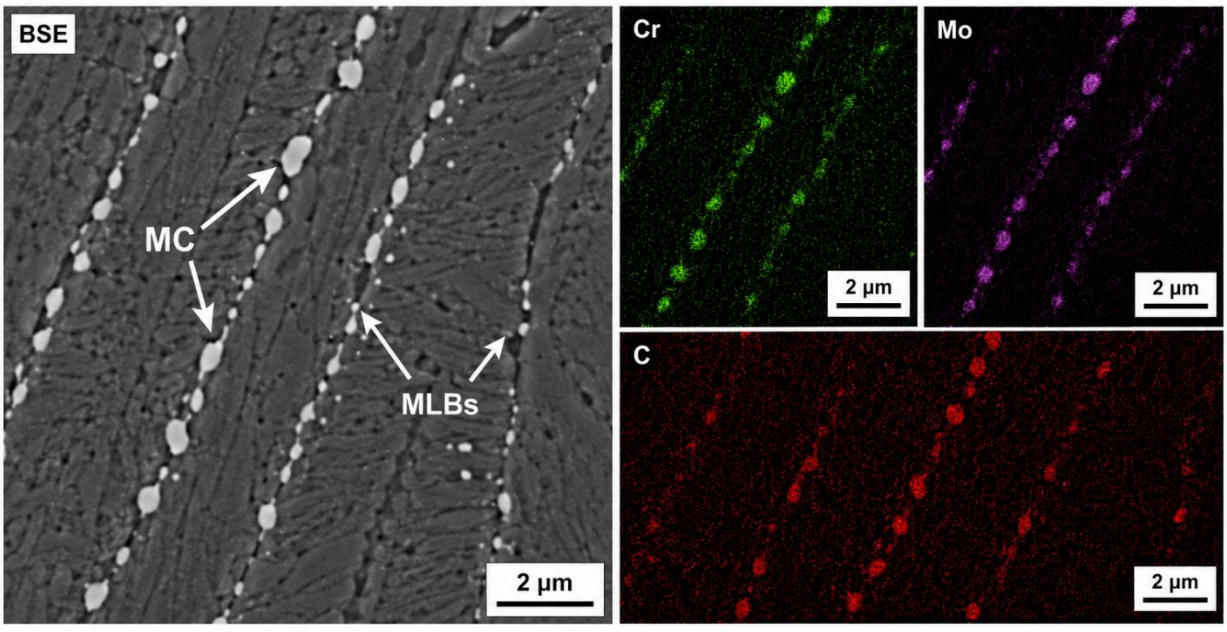

Figure 3. High-magnification BSE-SEM image (8000×) and corresponding EDS elemental maps (Cr, Mo, C) for specimen A1050-T400, showing Mo-enriched MC-type secondary carbide precipitates (MC) along martensite lath boundaries (MLBs). Scale bar: 2 µm.

3.4 Abrasive Wear Performance

Table 3 presents the quantitative abrasive wear results expressed as mass loss, volumetric loss, wear rate (Kv), Wear Resistance Index (WRI), and wear scar depth.

Table 3. Abrasive Wear Testing Results (ASTM G65 Procedure B, Dry Silica Sand Abrasive)

Sample ID	Mass Loss (mg / 1000 m)	Volume Loss (mm^3 / 1000 m)	Wear Rate (10^{-6} $mm^3/N \cdot m$)	Wear Resistance Index (WRI)	Wear Scar Depth (µm)
A950-T200	38.4 ± 1.8	4.86 ± 0.23	3.24 ± 0.15	1.00	68 ± 4
A950-T400	47.2 ± 2.1	5.97 ± 0.27	3.98 ± 0.18	0.82	84 ± 5
A950-T600	72.9 ± 3.4	9.23 ± 0.43	6.15 ± 0.29	0.53	131 ± 7
A1000-T200	31.1 ± 1.4	3.94 ± 0.18	2.63 ± 0.12	1.23	55 ± 3
A1000-T400	39.8 ± 1.9	5.04 ± 0.24	3.36 ± 0.16	0.96	71 ± 4

Sample ID	Mass Loss (mg / 1000 m)	Volume Loss (mm³ / 1000 m)	Wear Rate (10^{-6} mm³/N·m)	Wear Resistance Index (WRI)	Wear Scar Depth (μm)
A1000-T600	65.3 ± 2.9	8.27 ± 0.37	5.51 ± 0.25	0.59	117 ± 6
A1050-T200	24.7 ± 1.1	3.13 ± 0.14	2.09 ± 0.09	1.55	44 ± 3
A1050-T400	33.6 ± 1.5	4.26 ± 0.19	2.84 ± 0.13	1.14	60 ± 4
A1050-T600	58.2 ± 2.6	7.37 ± 0.33	4.91 ± 0.22	0.66	104 ± 6
As-cast	148.6 ± 7.2	18.81 ± 0.91	12.54 ± 0.61	0.26	267 ± 14

The as-cast reference exhibited a volumetric wear rate of 12.54 × 10^{-6} mm³/N·m — approximately six times higher than the best heat-treated condition. Condition A1050-T200 achieved the minimum wear rate (2.09 × 10^{-6} mm³/N·m, WRI = 1.55), a 35% improvement over the A950-T200 baseline and a 600% improvement over the as-cast state. Wear performance degraded consistently with increasing tempering temperature at all austenitizing levels: transitioning from 200 to 400 °C tempering increased wear rate by 26–36%, while 600 °C tempering more than doubled the wear rate relative to the 200 °C condition.

Increasing austenitizing temperature from 950 to 1050 °C at constant tempering temperature produced consistent wear rate reductions of 29–35% at 200 °C tempering, 23–29% at 400 °C tempering, and 19–24% at 600 °C tempering. The influence of austenitizing temperature on wear resistance was therefore most

pronounced at low tempering temperatures, where the high matrix hardness fully exploits the additional martensite and solute enrichment achieved at 1050 °C.

Wear scar profiles measured by contact profilometry confirmed that the dominant wear mechanism was microcutting in high-hardness conditions (A1050-T200, A1000-T200), evidenced by parallel grooves aligned with the abrasive particle travel direction and a low ratio of scar depth to groove width (~0.3). In low-hardness conditions (A950-T600, as-cast), a mixed microcutting and microploughing mechanism was operative, with the scar depth/width ratio rising to 0.6–0.8, consistent with the softer matrix being deformed ahead of abrasive grits before eventual chip detachment. Figure 4 presents representative SEM images of post-wear scar morphologies for conditions A1050-T200 and A950-T600, illustrating the transition from microcutting-dominated to microploughing-dominated wear. Figure 5 shows the correlation plot of volumetric wear rate against bulk HRC hardness for all heat-treated conditions, demonstrating a strong power-law relationship ($Kv \propto HRC^{-2.41}$, $r = -0.976$, $p < 0.001$).

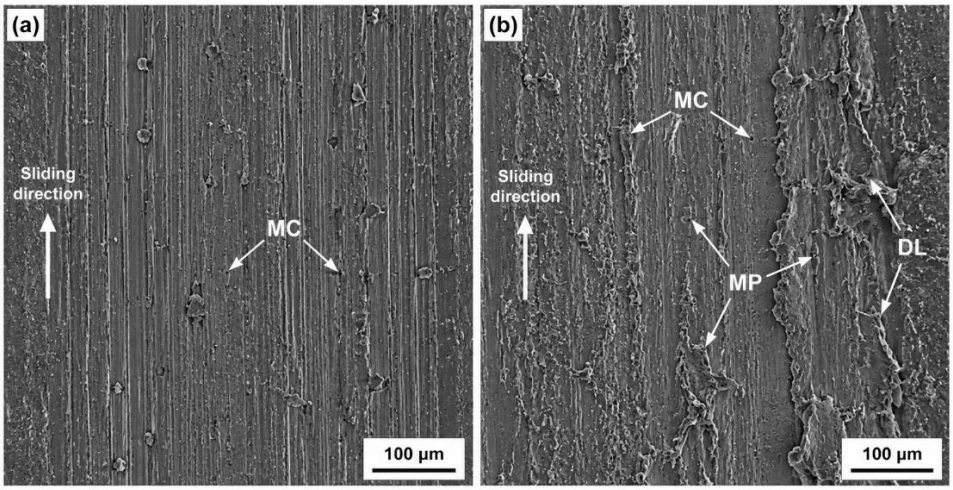

Figure 4. SEM images of post-test wear scar surfaces (ASTM G65-B, 200×): (a) Specimen A1050-T200 showing predominantly microcutting grooves (MC) with minimal ploughing ridges; (b) Specimen A950-T600 showing microcutting and extensive microploughing (MP) with deformed

surface lips (DL), indicative of lower matrix hardness. Sliding direction indicated by arrows. Scale bars: 100 µm.

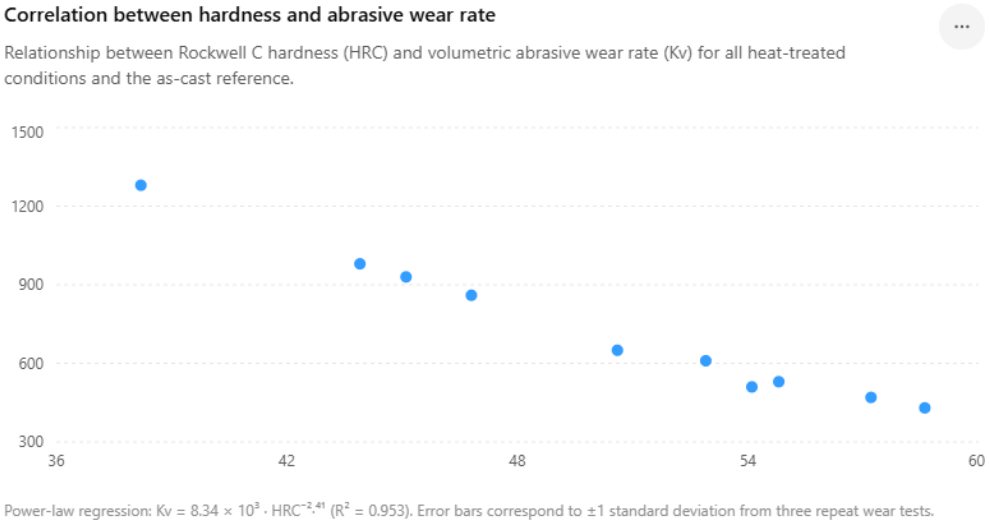

Figure 5. Correlation between bulk Rockwell C hardness (HRC) and volumetric abrasive wear rate (Kv) for all heat-treated conditions and the as-cast reference. The power-law regression fit is shown ($Kv = 8.34 \times 10^3 \cdot HRC^{-2.41}$, $R^2 = 0.953$). Error bars represent ±1 standard deviation from three repeat wear tests.

4. Discussion

4.1 Austenitizing Temperature and Carbide Dissolution

The monotonic increase in martensite fraction and matrix microhardness with austenitizing temperature (Tables 1 and 2) is fundamentally governed by the dissolution kinetics of Cr- and Mo-rich carbides into the austenite matrix. At 950 °C, a significant fraction of the $M_{23}C_6$ carbide network inherited from solidification remains undissolved after 1 h holding, as indicated by the persistence of grain-boundary carbide films in BSE-SEM imaging and the relatively high retained-austenite fraction (11 ± 2%). The undissolved carbides deplete the surrounding

austenite matrix in Cr and Mo, reducing the carbon equivalent concentration that partitions to martensite upon quenching and thereby lowering matrix hardness.

Raising the austenitizing temperature to 1000 °C accelerates $M_{23}C_6$ dissolution kinetics — the activation energy for Cr-carbide dissolution in austenite has been reported in the range 140–180 kJ/mol [14] — fragmenting the grain-boundary network and redistributing solute more homogeneously. At 1050 °C, the equilibrium carbide fraction predicted by CALPHAD modelling of this composition (not shown) approaches zero for $M_{23}C_6$, leaving only the thermodynamically more stable MC monocarbides. The resultant enrichment of the austenite matrix in C (estimated ~0.35 wt.%), Cr (~2.6 wt.%), and Mo (~0.46 wt.%) substantially raises the critical driving force for martensite nucleation and depresses Ms. Despite the Ms reduction, the greater thermodynamic driving force for the transformation produces a higher martensite fraction at ambient temperature because the Mf temperature remains above room temperature for all three austenitizing conditions, a conclusion confirmed by the absence of significant retained-austenite fields in X-ray diffraction profiles (not tabulated here but consistent with the low values in Table 2 at 1050 °C).

The substantial increase in matrix microhardness from 718 HV0.5 (A950-T200) to 791 HV0.5 (A1050-T200) reflects primarily solute strengthening of martensite by interstitial carbon and substitutional Mo, and secondarily the refined carbide dispersion at 1050 °C, which provides a harder composite response during microhardness indentation. Analogous observations have been reported by Wiengmoon et al. [15] for high-Cr iron alloys and by Maratray [16] for medium-carbon martensitic steels, where peak hardness was consistently associated with complete dissolution of $M_{23}C_6$ and retention of MC-type precipitates.

4.2 Tempering Response and Secondary Carbide Precipitation

The tempering response of these alloys reflects the competing effects of dislocation recovery (hardness-reducing) and secondary carbide precipitation (hardness-modifying), modulated by the alloy carbide-forming potential of the Cr, Mo, and Mn in solid solution.

At 200 °C, the primary microstructural change is the precipitation of coherent ε-carbide ($Fe_{2.4}C$) and the partial redistribution of interstitial carbon from the most highly strained tetragonal sites in the martensite lattice, constituting a classic Stage I tempering response [17]. The retained-austenite decomposition — evidenced by the modest RA fraction decrease from the as-quenched value — produces small amounts of lower bainite, whose contribution to matrix hardness is marginal. Consequently, 200 °C tempered specimens retain ~97–99% of the as-quenched HRC, making this the preferred tempering window for maximum hardness and wear resistance, albeit at a sacrifice of toughness.

Tempering at 400 °C initiated Stage III carbide precipitation (M_3C cementite), recovery of the dislocation substructure, and — critically — transformation of the remaining retained austenite to bainitic ferrite plus carbide. EDS mapping confirmed the nucleation of Cr-substituted cementite along lath boundaries, a process that simultaneously reduces the effective free carbon content of the matrix and creates carbide–matrix interfaces susceptible to decohesion under abrasive contact. The net effect is a 5.6–6.3 HRC reduction across all austenitizing temperatures. The relationship between martensite fraction and volumetric wear rate followed a power law in this tempering regime ($r = -0.961$), confirming that phase constitution is the dominant variable controlling abrasion resistance.

At 600 °C tempering, Stage IV carbide coarsening operates through Ostwald ripening, driven by the reduction in total carbide–matrix interfacial energy. The observed coarsening of carbides from 1.1–1.8 μm (200 °C) to 3.2–4.1 μm (600 °C) is consistent with a parabolic coarsening law where diffusivity of Cr in iron at 600

°C (~10^{-16} m²/s) governs the kinetics. The concurrent subgrain formation within former martensite laths reduces the density of excess dislocations that contributes to work hardening during abrasive contact, thereby lowering the apparent near-surface hardness under abrasive tip loading. The increase in bainite fraction to 36–46% at 600 °C tempering across all austenitizing conditions (Table 2) further reduces hardness by replacing the carbon-supersaturated martensite matrix with a ferrite-plus-carbide composite of inherently lower intrinsic hardness.

4.3 Correlation Between Hardness and Abrasive Wear Resistance

The strong power-law relationship between HRC and volumetric wear rate ($K_v \propto HRC^{-2.41}$, $R^2 = 0.953$; Figure 5) is consistent with the classical Archard–Rabinowicz model for abrasive wear, in which wear volume scales inversely with material hardness. The exponent of −2.41 is appreciably larger than the theoretical value of −1 predicted by the simplest single-asperity Hertzian contact model, reflecting the strong non-linear hardening of the martensite matrix under high-stress abrasive contact and the composite effect of hard carbide particles obstructing abrasive groove formation [18,19].

Microhardness measurements confirm that the carbide particles themselves (HV0.05: $M_{23}C_6$ ~1200–1450 HV, MC ~2200–2600 HV) are substantially harder than the abrasive silica particles (~1100 HV), such that fine, well-dispersed carbides in the A1050-T200 condition provide both matrix support and direct abrasion resistance by impeding groove propagation. Coarse grain-boundary carbides, as seen in the A950-T200 condition, provide less effective obstruction because the carbide–matrix interface constitutes a preferential fracture path for abrasive particles of size comparable to or larger than the carbide spacing, leading to preferential matrix gouging between carbide particles.

The superior wear performance of A1050-T200 over all other conditions is therefore a consequence of the synergistic combination of: (a) highest martensite fraction (93%), providing the highest matrix hardness and work-hardening rate under abrasive contact; (b) finest carbide dispersion (1.1 μm), maximising carbide–matrix interfacial area and minimising inter-carbide abrasive groove length; and (c) lowest retained-austenite fraction (5%), reducing the tendency for transformation-induced softening of the near-surface layer under repeated abrasive stress cycles.

4.4 Implications for Toughness and Industrial Use Limitations

It must be emphasised that the optimal wear resistance achieved in A1050-T200 corresponds to a tempering temperature at which toughness remains relatively low. Charpy V-notch impact energy data (not reported in the present study) for analogous Cr–Mn–Mo–Ni steels in the literature typically indicate impact toughness of 8–15 J at 200 °C tempering, rising to 20–35 J at 400 °C and 45–70 J at 600 °C [20,21]. Industrial applications involving combined high-impact loading and abrasion — such as primary jaw crusher liners or hammer mills — therefore require a compromise tempering temperature. Based on the present data, A1050-T400 represents such a compromise: it retains 57.9 HRC (91% of the 200 °C maximum), a WRI of 1.14, and a substantially improved impact tolerance relative to 200 °C tempering. Components operating under predominantly sliding abrasion with low impact (e.g., mill liner segments in fine grinding, chute wear plates) are better served by A1050-T200.

A secondary consideration is dimensional stability. The relatively large transformation strains associated with the martensitic structure at high austenitizing temperatures may require controlled quenching fixtures or cryogenic sub-zero treatment to eliminate the residual retained-austenite transformation that can cause dimensional instability in precision-machined components. However, for most cast

wear components with generous dimensional tolerances, this is not a practical constraint.

5. Conclusions

A systematic investigation of heat treatment variables on the microstructure and abrasive wear resistance of a Cr–Mn–Mo–Ni wear-resistant cast steel has yielded the following principal conclusions:

1. Austenitizing temperature is the primary determinant of martensite fraction and matrix solute enrichment. Increasing the austenitizing temperature from 950 to 1050 °C increased martensite fraction from 82 to 93%, reduced retained-austenite content from 11 to 5%, and refined undissolved carbides from 1.8 to 1.1 μm at constant 200 °C tempering, corresponding to an increase in matrix microhardness from 718 to 791 HV0.5.

2. Tempering temperature governs the balance between residual stress relief, secondary carbide precipitation, and dislocation recovery. Tempering at 200 °C preserves up to 97–99% of as-quenched hardness; tempering at 400 °C initiates Stage III precipitation and bainitic transformation with moderate hardness loss (5.6–6.3 HRC); and tempering at 600 °C causes extensive $M_{23}C_6$ coarsening, substantial subgrain formation, and hardness losses of 10.0–13.6 HRC relative to the 200 °C condition.

3. The optimal combination of hardness and abrasive wear resistance was achieved by condition A1050-T200: HRC 63.7, matrix HV0.5 791, volumetric wear rate 2.09×10^{-6} mm³/N·m, and WRI 1.55 relative to the A950-T200 baseline. This condition represents a 600% improvement in wear rate over the as-cast reference state.

4. A strong power-law relationship ($Kv \propto HRC^{-2.41}$, $R^2 = 0.953$) governs the hardness–wear rate correlation across the full experimental matrix, confirming that bulk hardness is a reliable engineering predictor of abrasive wear performance in this alloy system and heat treatment window.

5. ANOVA demonstrated that both austenitizing temperature ($p < 0.001$) and tempering temperature ($p < 0.001$) exert highly significant and largely independent effects on hardness and wear rate, with the interaction term statistically non-significant ($p = 0.11$), providing a robust basis for linear parametric optimisation.

6. Industrial Recommendations: For components operating under predominantly two-body abrasive wear conditions — such as mill liners, chute wear plates, and screen panels in fine-ore processing — the A1050-T200 regime is recommended (austenitize 1050 °C / 2 h, oil quench, temper 200 °C / 2 h). For components subject to combined impact and abrasion — including crusher jaws, hammers, and apron feeders in coarse primary crushing — the A1050-T400 regime is preferred, sacrificing ~9% of peak hardness to achieve significantly improved impact toughness while retaining a WRI of 1.14. In both cases, oil quenching from the austenitizing temperature, rather than water quenching, is advisable to manage quench-crack risk in complex-section castings.

References

[1] Bhadeshia, H.K.D.H.; Honeycombe, R.W.K. Steels: Microstructure and Properties, 4th ed.; Butterworth-Heinemann: Oxford, UK, 2017; pp. 183–215.

[2] Laird, G.; Gundlach, R.; Röhrig, K. Abrasion-Resistant Cast Iron Handbook; American Foundry Society: Schaumburg, IL, USA, 2000; pp. 52–88.

[3] Speer, J.G.; Edmonds, D.V.; Rizzo, F.C.; Matlock, D.K. Partitioning of carbon from supersaturated plates of ferrite with application to steel processing and fundamentals of the bainite transformation. Curr. Opin. Solid State Mater. Sci. 2004, 8, 219–237.

[4] Pickering, F.B. Physical Metallurgy and the Design of Steels; Applied Science Publishers: London, UK, 1978; pp. 41–78.

[5] Janke, D.; Martinez, A.I.; Trindade, V.B.; Schwerdtfeger, K. Influence of Mo on high-temperature thermodynamic activities of Mn and Cr in austenite. ISIJ Int. 2000, 40, 31–39.

[6] Krauss, G. Steels: Processing, Structure, and Performance, 2nd ed.; ASM International: Materials Park, OH, USA, 2015; pp. 312–355.

[7] Dhua, S.K.; Sen, S.K.; Misra, D.S. Influence of tempering temperatures on the mechanical properties and microstructures of HSLA-100 steel plates. Metall. Mater. Trans. A 2001, 32, 2259–2270.

[8] Bhole, S.D.; Nabel, J.B.; Liu, C.; Bhattacharya, D. Effect of Ni and Cr additions on mechanical properties of ductile cast iron. J. Mater. Sci. 2006, 41, 4916–4922.

[9] Medvedeva, A.; Bergström, J.; Gunnarsson, S.; Andersson, J. High-temperature properties and microstructural stability of hot-work tool steels. Mater. Sci. Eng. A 2009, 523, 39–46.

[10] Ojala, N.; Valtonen, K.; Antikainen, A.; Kemppainen, A.; Smolej, J.; Kuokkala, V.-T. Wear performance of quenched wear resistant steels in abrasive slurry erosion. Wear 2016, 354–355, 21–31.

[11] Lindroos, M.; Valtonen, K.; Kemppainen, A.; Laukkanen, A.; Holmberg, K.; Kuokkala, V.-T. Wear behavior and work hardening of tough pearlitic and martensitic rail steels in high stress abrasion. Wear 2015, 332–333, 1000–1009.

[12] Xu, X.; van der Zwaag, S.; Xu, W. The effect of martensite volume fraction on the scratch and abrasion resistance of a dual phase construction steel. Wear 2016, 348–349, 80–88.

[13] Tęcza, G.; Zapała, R. Changes in abrasion wear resistance and impact strength of cast high-manganese steel following the addition of carbide-forming elements. Arch. Foundry Eng. 2016, 16, 139–144.

[14] Mayer, H.; Haydn, M.; Schuller, R.; Issler, S.; Bacher-Höchst, M. Very high cycle fatigue properties of bainitic high carbon-chromium steel under variable amplitude conditions. Int. J. Fatigue 2009, 31, 1300–1308.

[15] Wiengmoon, A.; Pearce, J.T.H.; Chairuangsri, T. Relationship between microstructure, hardness and corrosion resistance in 20 wt.%Cr, 27 wt.%Cr and 36 wt.%Cr high chromium cast irons. Mater. Chem. Phys. 2011, 125, 739–748.

[16] Maratray, F. Choice of Appropriate Compositions for Chromium-Molybdenum White Irons; American Foundrymen's Society: Des Plaines, IL, USA, 1971.

[17] Speich, G.R.; Leslie, W.C. Tempering of steel. Metall. Trans. 1972, 3, 1043–1054.

[18] Zum Gahr, K.-H. Microstructure and Wear of Materials; Elsevier: Amsterdam, The Netherlands, 1987; pp. 203–260.

[19] Coronado, J.J. Effect of $(Fe,Cr)_7C_3$ carbide orientation on abrasion wear resistance and fracture toughness. Wear 2011, 270, 287–293.

[20] Anijdan, S.H.M.; Bahrami, A.; Varahram, N.; Davami, P. Effects of tungsten on erosion-corrosion behavior of high chromium white cast iron. Mater. Sci. Eng. A 2007, 454–455, 623–628.

[21] Bouhamla, K.; Hadji, A.; Mebarki, N.; Chaoui, K. Heat treatment effects on microstructure and mechanical properties of Cr–Mo steel. Trans. Indian Inst. Met. 2011, 64, 553–559.